

Anomalous High-Field Magnetotransport in CaFeAsF due to the Quantum Hall Effect

Taichi Terashima,^{1,*} Hishiro T. Hirose,² Naoki Kikugawa,³ Shinya Uji,¹ David Graf,⁴ Takao Morinari,⁵ Teng Wang,^{6,7} and Gang Mu^{6,7,†}

¹*International Center for Materials Nanoarchitectonics,
National Institute for Materials Science, Tsukuba 305-0003, Japan*

²*Research Center for Functional Materials,
National Institute for Materials Science, Tsukuba 305-0003, Japan*

³*Center for Green Research on Energy and Environmental Materials,
National Institute for Materials Science, Tsukuba, Ibaraki 305-0003, Japan*

⁴*National High Magnetic Field Laboratory,
Florida State University, Tallahassee, FL 32310, USA*

⁵*Course of Studies on Materials Science,
Graduate School of Human and Environmental Studies,
Kyoto University, Kyoto 606-8501, Japan*

⁶*State Key Laboratory of Functional Materials for Informatics,
Shanghai Institute of Microsystem and Information Technology,
Chinese Academy of Sciences, Shanghai 200050, China*

⁷*CAS Center for Excellence in Superconducting
Electronics (CENSE), Shanghai 200050, China*

(Dated: July 23, 2021)

The discovery of iron-based superconductors [1] caused great excitement, as they were the second high- T_c materials after cuprates. Because of a peculiar topological feature of the electronic band structure [2, 3], investigators quickly realized that the antiferromagnetic parent phase harbors Dirac fermions. Here we show that the parent phase also exhibits the quantum Hall effect. We determined the longitudinal and Hall conductivities in CaFeAsF up to a magnetic field of 45 T and found that both approach zero above 40 T. CaFeAsF has Dirac electrons and Schrödinger holes [4], and our analysis indicates that the Landau-level filling factor $\nu = 2$ for both at these high field strengths. We therefore argue that the $\nu = 0$ quantum Hall state emerges under these conditions. Our finding of quantum Hall physics at play in a topologically nontrivial parent phase adds a new dimension to research on iron-based superconductors and also provides a new material variety for the study of the $\nu = 0$ quantum Hall state.

CaFeAsF is a variant of 1111 iron-based superconductor parent compounds, in which the LaO in LaFeAsO is replaced with CaF. Unlike LaFeAsO, large high-quality single crystals of CaFeAsF can be grown [5]; hence, it is suitable for studying electronic structure. As Ran *et al.* [2] argued, the spin-density-wave gap in the antiferromagnetic ground state cannot be fully open but it should have a node. Accordingly, the Fermi surface of CaFeAsF is composed of a symmetry-related pair of α Dirac electron cylinders and a β Schrödinger hole cylinder [Fig. 1(c)] [4]. The carrier density is very small, of the order of 10^{-3} per Fe (Table 1). As expected from the Fermi surface, CaFeAsF exhibits highly two-dimensional electronic conduction with an anisotropy ratio of 200–300 between the c -axis and ab -plane resistivities. Previously, Ma *et al.* performed resistivity measurements on CaFeAsF up to $B = 65$ T [6]. They found that the resistivity increased sharply for fields above $B \sim 30$ T applied along the c axis at low temperatures and that the temperature dependence became nonmetallic in the high-field region. Based on a scaling analysis, they argued that a metal–insulator quantum phase transition occurred at $B_c = 30$ T. In this work, we measured not only the longitudinal resistivity ρ_{xx} but also the Hall resistivity ρ_{yx} in CaFeAsF up to $B = 45$ T; we argue that the high-field insulating phase is the $\nu = 0$ quantum Hall state.

Single crystals of CaFeAsF were prepared at the SIMIT in Shanghai via a CaAs self-flux method [5]. We first measured Shubnikov–de Haas (SdH) oscillations in the main sample (named D2) used for the present study, employing a 20-T superconducting magnet and a dilution refrigerator at the NIMS in Tsukuba to determine the Fermi-surface parameters

(Fig. 1). Two frequency peaks corresponding to the α Dirac electron and β Schrödinger hole cylinders appear in the Fourier transform of the second-derivative curve as a function of $1/B$ [Fig. 1(b)]. We determined the effective masses m^* for $B \parallel c$ from the temperature dependences of the peak amplitudes. To extract the frequencies F and Dingle temperatures T_D , we then fitted the Lifshitz–Kosevich formula [7, 8] to the lowest-temperature data with the effective masses fixed [9]. The obtained parameters (Table 1) are consistent with our previous reports [4, 9]. The conduction-electron g factors in Table 1 are based on [4], which showed from the field-angle dependence of the SdH oscillations that the spin-splitting parameter $S = (1/2)g(m^*(\theta)/m_e)$ [8] was 1/2 and 5/2 for α and β , respectively, at $\theta \approx 50^\circ$. Here, θ is the field angle measured from the c axis, and the relation $m^*(\theta) = m^*(0)/\cos\theta$ holds for cylindrical Fermi surfaces. We obtained the tabulated g values using the value of $m^*(0)$ determined above.

We prepared a Landau-level diagram based on these parameters, as shown in Fig. 1(d). The shadings around the levels represent the Landau-level broadening Γ due to impurity scattering derived from the Dingle temperature. Although the shadings overlap with each other under low fields, the Landau levels are well separated near and above $B = 40$ T. We also show the Fermi level above $B = 20$ T (dashed line), neglecting level broadening. Note that the α Dirac electrons enter the quantum limit above $B \sim 30$ T where only the lowest Landau levels, $\alpha 0+$ and $\alpha 0-$, are occupied.

Figure 2 shows our main result. We simultaneously measured the longitudinal resistivity ρ_{xx} and Hall resistivity ρ_{yx} for sample D2 in fields up to $B = 45$ T applied along the c axis using a hybrid magnet at the NHMFL in Tallahassee. To eliminate mixing of the two components, we performed measurements in both positive and negative fields by rotating the sample by 180° and symmetrized and antisymmetrized ρ_{xx} and ρ_{yx} , respectively. As reported previously [6], the longitudinal resistivity increases rapidly above $B \sim 30$ T as the temperature is reduced. The value of ρ_{xx} at $B = 45$ T and $T = 0.4$ K is 265 times larger than the zero-field value. Because an anomalous resistivity increase is also observed for ρ_{zz} (i.e., $I \parallel B \parallel c$), as measured on sample X2 and shown in Fig. 3(b), it cannot be ascribed to classical magnetoresistance because of the orbital motions of the carriers.

The Hall resistivity above $B \sim 30$ T is positive at $T = 10$ and 5 K but becomes negative at $T = 1.6$ and 0.4 K [Fig. 2(b)]. Within the semiclassical magnetotransport theory, the Hall resistivity in the high-field limit is determined by the net number of carriers: $\rho_{yx} =$

$B/(e(p-n))$, where n and p are the densities of electrons and holes, respectively. This gives $\rho_{yx} = 5.2 \text{ m}\Omega\text{cm}$ at $B = 45 \text{ T}$. Thus, the observed sign change is difficult to explain within the semiclassical theory. In addition, the magnitude of the experimental Hall resistivity is considerably smaller than the theoretical expectation at all temperatures. In summary, neither ρ_{xx} nor ρ_{yx} above $B \sim 30 \text{ T}$ can be explained by the semiclassical theory.

Figure 2(c) shows the longitudinal conductivity σ_{xx} and the Hall conductivity σ_{xy} , which are given respectively by $\sigma_{xx} = \rho_{xx}/(\rho_{xx}^2 + \rho_{yx}^2)$ and $\sigma_{xy} = \rho_{yx}/(\rho_{xx}^2 + \rho_{yx}^2)$. In this figure, we also show the conductivity corresponding to one conductance quantum e^2/h per FeAs layer. This figure gives a better perspective on the high-field magnetotransport in CaFeAsF. Note that both σ_{xx} and σ_{xy} at $B = 45 \text{ T}$ are much smaller than e^2/h , and they approach zero as the temperature is reduced.

We now return to Fig. 1(d). The α electrons are in the quantum limit above $B \sim 30 \text{ T}$. The filling factor ν_α is calculated to be 2; the lowest Landau level of the Dirac electrons is special and contributes 1/2 to the filling factor. Because there are two α cylinders in the Brillouin zone and two spin species, the sum of their contributions becomes 2. For the β holes, the β_{0+} level becomes less-than-half filled above $B \sim 38 \text{ T}$, and hence, the Fermi level exists among localized tail states. Accordingly, the two fully filled levels β_{0-} and β_{1-} give the filling factor $\nu_\beta = 2$. As the total filling factor $\nu = \nu_\beta - \nu_\alpha$ [10] is zero, we expect both σ_{xx} and σ_{xy} to approach zero as the quantum Hall state develops. This explains our observations.

Usually, in quantum Hall states ($\nu \neq 0$), $\sigma_{xx} = 0$ but σ_{xy} remains finite ($= \nu e^2/h$). Therefore, $\rho_{xx} = 0$ and $\rho_{yx} = h/(\nu e^2)$. However, when $\nu = 0$, σ_{xy} is also expected to approach zero. Accordingly, the way ρ_{xx} and ρ_{yx} behave depends on the detailed behavior of σ_{xx} and σ_{xy} . The $\nu = 0$ quantum Hall state has been studied in InAs/GaSb systems [11, 12], HgTe quantum wells [13], and graphene devices [14, 15]. In the first two systems, electrons and holes coexist, while in graphene the $\nu = 0$ state is achieved by tuning the Fermi level to the Dirac point. Reported observations may be summarized as follows: In the InAs/GaSb systems, where imbalances exist between the electron and hole carriers, σ_{xy} is much closer to zero than σ_{xx} at $\nu = 0$. In the latter two systems, σ_{xy} even crosses zero as the (net) carrier polarity is varied by the gate voltage. In all the three systems, ρ_{xx} at $\nu = 0$ increases strongly with the magnetic field as the temperature is reduced. However, the temperature dependence of ρ_{xx} is much weaker than that due to thermal activation and

exhibits saturation at low temperatures, suggesting that σ_{xx} remains finite as $T \rightarrow 0$.

We show the temperature dependence of ρ_{xx} at $B = 45$ T as a function of temperature in Fig. 3(a). Because sample D2 was measured only at four temperatures (the blue circles), we also plotted data from sample X1 (green squares). In the latter case, the magnetic field was applied at 9.2° off the c axis (for technical reasons), but this level of field tilting affects the resistivity only slightly, as can be seen in Fig. 3(b). The temperature dependence cannot be described by an activation form (inset); rather, it follows a T^{-1} dependence over a wide temperature range and then saturates at the lowest temperatures. This is similar to the behavior observed in the InAs/GaSb systems and in HgTe quantum wells [11, 13]. (Ma *et al.* observed a stronger temperature dependence up to $T^{-1.7}$ at higher fields, $B \sim 60$ T [6].) We also examined the temperature dependence of the c -axis resistivity ρ_{zz} measured in sample X2 (red circles). Although the c -axis conduction mechanism is unclear presently, ρ_{zz} exhibits essentially the same temperature dependence.

We also note additional similarities between the InAs/GaSb systems and CaFeAsF. The Hall resistivity in the InAs/GaSb systems shows stronger SdH oscillations than the longitudinal resistivity. The Hall resistivity shows neither a plateau nor a plateau-to-plateau transition, except for one Hall plateau at $\nu = 1$ [12]. The sign of the Hall resistivity near the high-field region $\nu = 0$ changes suddenly from positive to negative as the temperature is lowered from 1.8 to 0.5 K (the lower inset of Fig. 1 of [12]). For comparison, the Hall resistivity in CaFeAsF shows clear oscillations but neither a plateau nor a plateau-to-plateau transition. Above $B \sim 30$ T, the sign of the Hall resistivity changes as the temperature is reduced from 5 to 1.6 K.

Finally, we mention the field-angle dependence of the resistivity increase. Figure 3(b) shows the longitudinal resistivity in sample X1 for various field directions as a function of the c -axis component of the applied field $B \cos \theta$. The curves do not collapse into a single curve, as noted by [6]. This is essentially because the Zeeman energy is not determined by $B \cos \theta$, but by B .

There seems to be an interplay between the SdH oscillations and the $\nu = 0$ quantum Hall state. The SdH oscillations from up-spin and down-spin electrons interfere, resulting in a prefactor $R_s = \cos(\pi S)$ in the oscillation function. Because $S = 1/2$ and $5/2$ for α and β , respectively, at $\theta \approx 50^\circ$, R_s changes sign there for both oscillations, as confirmed by Fig. 3(b). For $\theta < 50^\circ$, the curves exhibit a minimum at $B \cos \theta \sim 19$ T and a maximum

at $B \cos \theta \sim 23$ T due to the α and β oscillations, respectively. For $\theta > 50^\circ$, however, the curves exhibit a maximum at $B \cos \theta \sim 19$ T and a minimum at $B \cos \theta \sim 23$ T. Although the SdH-oscillatory resistivity in the $B = 40\text{--}45$ T region is positive at small θ , as θ increases, it eventually becomes negative because of the sign change of R_s . This is probably related to the observed suppression of the resistivity increase as θ is increased.

The quantum Hall effect in bulk materials has been reported, for example, for organic Bechgaard salts [16–19] and $\eta\text{-Mo}_4\text{O}_{11}$ [20], EuMnBi_2 [21], highly doped Bi_2Se_3 [22], and ZrTe_5 [23]. Interestingly, in the Bechgaard salts spin-density-wave formation removes most of the Fermi surface, leaving only tiny two-dimensional pockets, which give rise to the quantum Hall effect. This is analogous to the case of CaFeAsF , in which the spin-density-wave gap cannot be fully open and tiny cylindrical Fermi pockets remain to exhibit the quantum Hall effect. However, the $\nu = 0$ state has been studied only in two-dimensional systems thus far. CaFeAsF is the first bulk material to exhibit the $\nu = 0$ state. Studies comparing CaFeAsF with two-dimensional systems are thus expected to be fruitful.

ACKNOWLEDGMENTS

This work was supported in Japan by JSPS KAKENHI Grant Numbers 17K05556. This work was supported in China by the Youth Innovation Promotion Association of the Chinese Academy of Sciences (No. 2015187). A portion of this work was performed at the National High Magnetic Field Laboratory, which is supported by the National Science Foundation Cooperative Agreement No. DMR-1644779 and the State of Florida.

REFERENCES

* TERASHIMA.Taichi@nims.go.jp

† mugang@mail.sim.ac.cn

- [1] Kamihara, Y., Watanabe, T., Hirano, M. & Hosono, H. Iron-Based Layered Superconductor $\text{La}[\text{O}_{1-x}\text{F}_x]\text{FeAs}$ ($x = 0.05\text{--}0.12$) with $T_c = 26$ K. *J. Am. Chem. Soc.* **130**, 3296 (2008).

- [2] Ran, Y., Wang, F., Zhai, H., Vishwanath, A. & Lee, D.-H. Nodal Spin Density Wave and Band Topology of the FeAs-Based Materials. *Phys. Rev. B* **79**, 014505 (2009).
- [3] Morinari, T., Kaneshita, E. & Tohyama, T. Topological and Transport Properties of Dirac Fermions in an Antiferromagnetic Metallic Phase of Iron-Based Superconductors. *Phys. Rev. Lett.* **105**, 037203 (2010).
- [4] Terashima, T. *et al.* Fermi Surface with Dirac Fermions in CaFeAsF Determined via Quantum Oscillation Measurements. *Phys. Rev. X* **8**, 011014 (2018).
- [5] Ma, Y. *et al.* Growth and Characterization of Millimeter-Sized Single Crystals of CaFeAsF. *Supercond. Sci. Technol.* **28**, 085008 (2015).
- [6] Ma, Y. *et al.* Magnetic-Field-Induced Metal-Insulator Quantum Phase Transition in CaFeAsF near the Quantum Limit. *Science China Physics, Mechanics & Astronomy* **61**, 127408 (2018).
- [7] Richards, F. E. Investigation of the Magnetoresistance Quantum Oscillations in Magnesium. *Phys. Rev. B* **8**, 2552–2571 (1973).
- [8] Shoenberg, D. *Magnetic Oscillations in Metals* (Cambridge University Press, Cambridge, 1984).
- [9] Terashima, T., Uji, S., Wang, T. & Mu, G. Topological Frequency Shift of Quantum Oscillation in CaFeAsF. *arXiv:2105.14733* (2021).
- [10] Mendez, E. E., Esaki, L. & Chang, L. L. Quantum Hall Effect in a Two-Dimensional Electron-Hole Gas. *Phys. Rev. Lett.* **55**, 2216–2219 (1985).
- [11] Daly, M. S. *et al.* Zero-Hall-Resistance State in a Semimetallic InAs/GaSb Superlattice. *Phys. Rev. B* **53**, R10524–R10527 (1996).
- [12] Nicholas, R. J. *et al.* Metal-Insulator Oscillations in a Two-Dimensional Electron-Hole System. *Phys. Rev. Lett.* **85**, 2364–2367 (2000).
- [13] Gusev, G. M. *et al.* Quantum Hall Effect near the Charge Neutrality Point in a Two-Dimensional Electron-Hole System. *Phys. Rev. Lett.* **104**, 166401 (2010).
- [14] Abanin, D. A. *et al.* Dissipative Quantum Hall Effect in Graphene near the Dirac Point. *Phys. Rev. Lett.* **98**, 196806 (2007).
- [15] Checkelsky, J. G., Li, L. & Ong, N. P. Zero-Energy State in Graphene in a High Magnetic Field. *Phys. Rev. Lett.* **100**, 206801 (2008).
- [16] Chaikin, P. M. *et al.* Tetramethyltetraselenafulvalenium Perchlorate, (TMTSF)₂ClO₄, in High Magnetic Fields. *Phys. Rev. Lett.* **51**, 2333–2336 (1983).

- [17] Ribault, M. *et al.* Quantum Hall Effect and Fermi Surface Instabilities in $(\text{TMTSF})_2\text{ClO}_4$. *J. Physique Lett.* **45**, 935–941 (1984).
- [18] Cooper, J. R. *et al.* Quantized Hall Effect and a New Field-Induced Phase Transition in the Organic Superconductor $(\text{TMTSF})_2\text{PF}_6$. *Phys. Rev. Lett.* **63**, 1984–1987 (1989).
- [19] Hannahs, S. T., Brooks, J. S., Kang, W., Chiang, L. Y. & Chaikin, P. M. Quantum Hall Effect in a Bulk Crystal. *Phys. Rev. Lett.* **63**, 1988–1991 (1989).
- [20] Hill, S. *et al.* Bulk Quantum Hall Effect in $\eta\text{-Mo}_4\text{O}_{11}$. *Phys. Rev. B* **58**, 10778–10783 (1998).
- [21] Masuda, H. *et al.* Quantum Hall Effect in a Bulk Antiferromagnet EuMnBi_2 with Magnetically Confined Two-Dimensional Dirac Fermions. *Science Advances* **2** (2016).
- [22] Cao, H. *et al.* Quantized Hall Effect and Shubnikov–de Haas Oscillations in Highly Doped Bi_2Se_3 : Evidence for Layered Transport of Bulk Carriers. *Phys. Rev. Lett.* **108**, 216803 (2012).
- [23] Tang, F. *et al.* Three-Dimensional Quantum Hall Effect and Metal–Insulator Transition in ZrTe_5 . *Nature* **569**, 537–541 (2019).

TABLE I. Fermi-surface parameters. The first three parameters F , m^* , and T_D were estimated from the Shubnikov–de Haas oscillations for $B \parallel c$ in sample D2; the numerical fitting errors are indicated. The rest were derived from these first three: n is the carrier density, v_F the Fermi velocity, E_F the Fermi energy, and $\Gamma = \pi k_B T_D$ the Landau-level broadening. The value of n for the α cylinder refers to the sum of the carriers of the two cylinders that occur in the Brillouin zone. To derive E_F , we used the linear dispersion relation ($E_F = \hbar v_F k_F$) for the α cylinder and a quadratic one ($E_F = \hbar^2 k_F^2 / (2m^*)$) for β . The conduction-electron g factor is based on [4].

FS cylinder	α	β
carrier type	Dirac electron	Schrödinger hole
F (T)	19.01(1)	47.50(2)
m^*/m_e	0.41(1)	0.91(2)
T_D (K)	4.80(5)	2.32(5)
n (10^{-3} per Fe)	1.39	1.74
n (10^{19} cm $^{-3}$)	2.14	2.68
v_F (10^4 m/s)	6.78	4.83
E_F (meV)	10.7	6.04
Γ (meV)	1.30	0.628
g	1.57	3.53

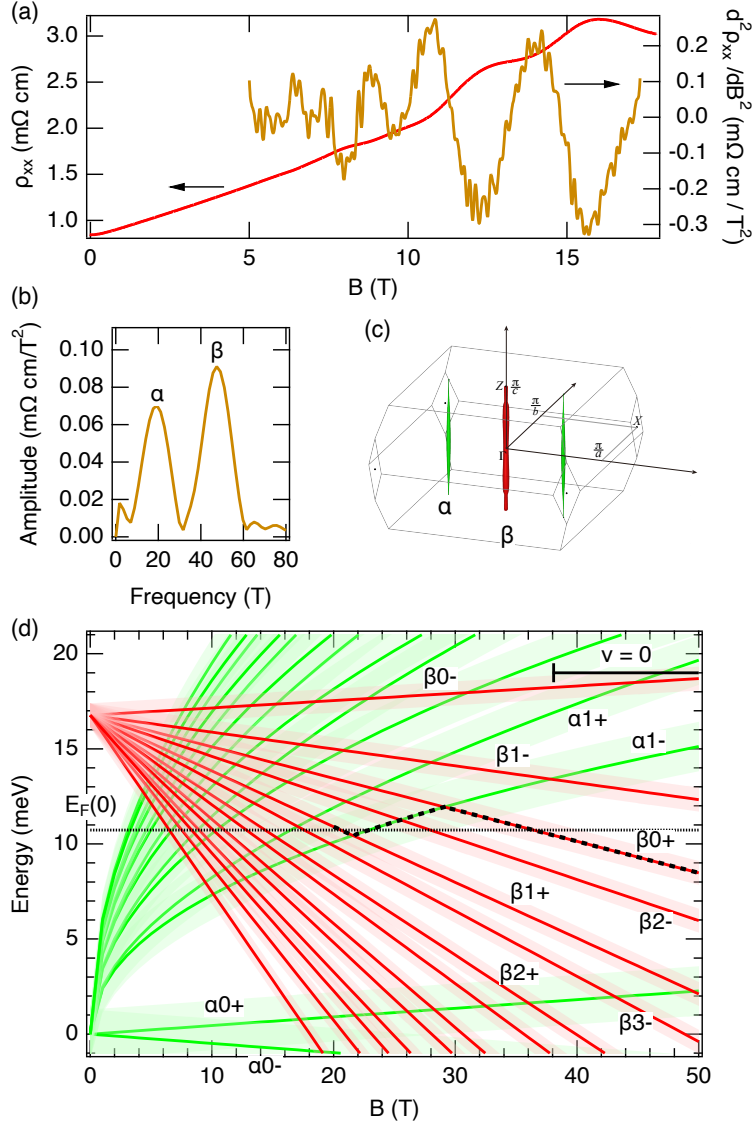


FIG. 1. Shubnikov–de Haas oscillations, the Fermi surface, and Landau levels in CaFeAsF (a) In-plane resistivity ρ_{xx} as a function of the magnetic field B applied along the c axis, as measured on sample D2 at $T = 0.03$ K. The corresponding second-derivative curve, $d^2\rho_{xx}/dB^2$, is also shown. (b) Fourier transform of the curve $d^2\rho_{xx}/dB^2$ considered as a function of $1/B$. Note that the unit of frequency in this case is tesla. The labels α and β refer to electrons and holes, respectively. (c) Fermi surface of CaFeAsF [4]. (d) Landau-level diagram for CaFeAsF calculated from the Fermi-surface parameters in Table 1. The shading around the levels is based on the Landau-level broadening Γ . The black dashed line above $B = 20$ T shows the field-dependent Fermi level when level broadening is neglected. Some of the levels are labeled with the carrier type (α or β), the Landau-level index (0, 1, etc.), and the spin species (+ or -). The horizontal bar shown at the upper right indicates the high-field region where $\nu = 0$.

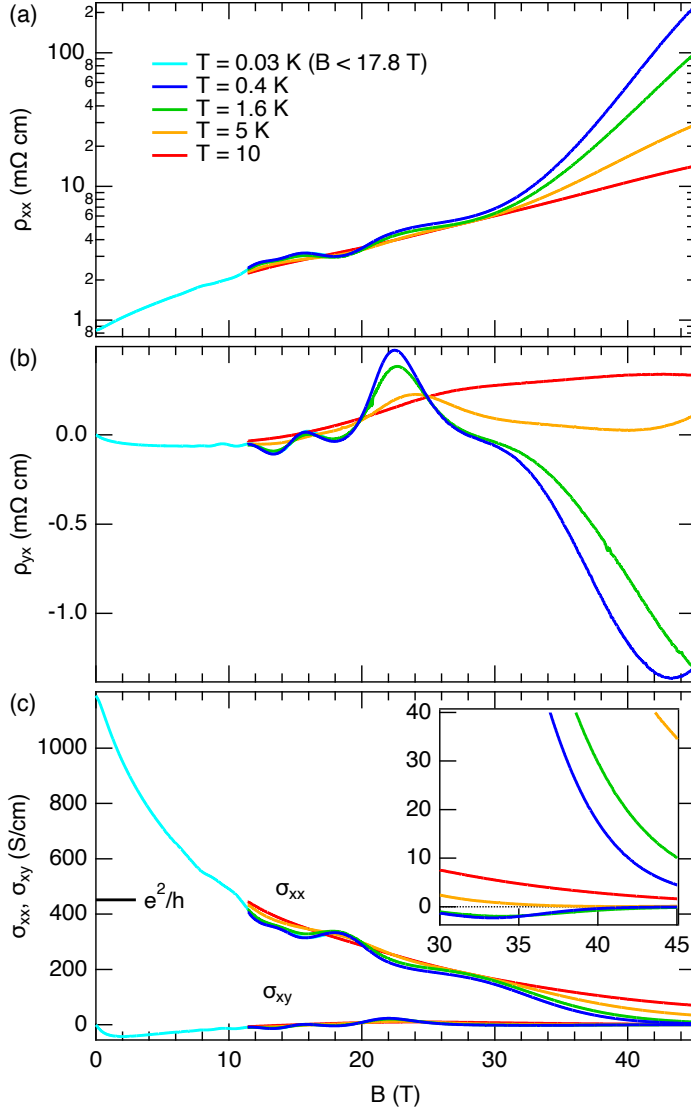


FIG. 2. Magnetotransport in CaFeAsF in fields up to $B = 45$ T applied along the c axis. (a) The longitudinal resistivity ρ_{xx} and (b) the Hall resistivity ρ_{yx} . (c) The longitudinal conductivity σ_{xx} and Hall conductivity σ_{xy} . The conductivity corresponding to one conductance quantum e^2/h per FeAs is indicated. The inset shows the blow-up of the high-field region.

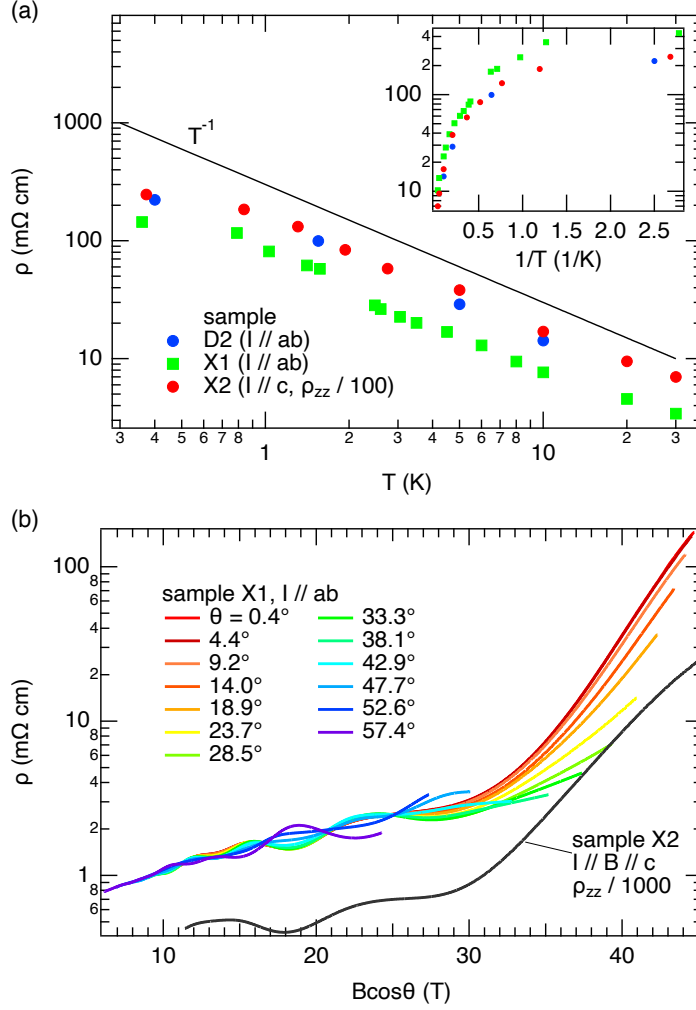


FIG. 3. Temperature and field-angle dependence of the high-field anomaly. (a) Resistivity at $B = 45$ T as a function of temperature. The field direction is $B \parallel c$ for samples D2 and X2 and $\theta = 9.2^\circ$ for X1. The inset shows an Arrhenius plot of the same data. (b) Resistivity of sample X1 for various field angles plotted against the c -axis component of the applied field $B \cos \theta$. The c -axis resistivity for $B \parallel c$ in sample X2 is also shown.